# MRI RF-induced Heating Prediction of Complexshaped Passive Implantable Medical Devices Using Mesh-based Convolutional Neural Network

Jiajun Chang, Qianlong Lan, Ran Guo, Jianfeng Zheng, Member, IEEE, Rebeca Romero, Wolfgang Kainz, Senior Member, IEEE, Stuart A. Long, Fellow IEEE, and Ji Chen, Senior Member, IEEE

Abstract— In this paper, a Convolutional Neural Network (CNN) model is proposed to predict the in-vitro radiofrequency (RF)-induced heating of complex-shaped passive implantable medical devices (PIMDs) under magnetic resonance imaging (MRI). The electromagnetic simulation meshes and incident electric field on the mesh grids are used as the input of the CNN model while the network output corresponds to the RF-induced 1-gram specific absorption rate (SAR). A convergence analysis is performed to understand the effectiveness of the method. A discussion on selecting the training dataset size is presented using a Principal Component Analysis (PCA) algorithm. Results demonstrate the robustness of the CNN model for the prediction of RF-induced heating from complex-shaped PIMDs under MR exposure.

Keywords—Magnetic Resonance Imaging (MRI), Passive Implantable Medical Devices (PIMD), Radiofrequency (RF)-induced heating, Convolutional Neural Network (CNN)

#### I. INTRODUCTION

COMPLEX-SHAPED passive implantable medical devices (PIMDs) are widely used in clinical treatments to support damaged biological tissues or structures [1]. However, PIMDs with metallic materials can lead to potential safety hazards when patients with PIMDs undergo magnetic resonance imaging (MRI) procedures [2]. Radiofrequency (RF)-induced heating is one of the major concerns. The concentrated radio frequency (RF) energy arising from the interactions between PIMDs and MRI RF electromagnetic (EM) fields will cause the temperature to rise and may burn human tissue [3]. Accordingly, RF-induced heating of PIMDs should be thoroughly evaluated to ensure patient safety [4]-[6].

The MRI RF exposure for PIMDs is usually assessed following the ASTM standard F2182-19e2 [7]. This assessment requires costly measurements or numerical simulations and takes a relatively long time [8]-[11]. Therefore, fast estimation of MRI RF exposure would be most beneficial to assessing the potential risks for patients with PIMDs.

Artificial Neural Networks (ANN) is one of the emerging techniques used in RF and microwave design [12]. It has been applied in a variety of applications, such as transmission line and waveguide modeling [13]-[15], and impedance matching [16]. Preliminary studies have demonstrated the potential of using a simple feed-forward ANN to predict the MRI RF-induced heating for simple shaped PIMDs which can be described by a set of geometrical parameters, such as the plate length, the plate width, and the number of screws [17]-[19]. However, practical PIMDs can have very complex structures and may be difficult to describe using a specific set of parameters. Therefore, the MRI RF-induced heating of PIMDs with complex shapes cannot be predicted accurately using existing methods [20]-[21].

Although complex-shaped PIMDs cannot be accurately described by a set of geometrical parameters, they can be well described using the computational meshes available in electromagnetic simulations [22]. However, this study assumed the uniform incident field so that the complex incident fields distribution on the device heating was not included in the study. Since the RF-induced heating is related both to the device (now represented by the simulation meshes) and to the incident field on the device, in this study, we propose to use the electromagnetic simulation meshes and the incident fields on the mesh grid as the inputs to develop a convolution neural network (CNN) model to predict the MRI RF exposure for complex-shaped PIMDs. Once the prediction CNN model is developed, to predict the RF-induced heating, one only needs to generate the electromagnetic simulation meshes and the incident field as the inputs to the CNN model for RF-induced heating evaluation. That is, instead of running electromagnetic simulations (requiring hours for each configuration), one can obtain the RF-induced heating for various new configurations within seconds using this surrogate model.

Four tibia systems are used for the CNN model development to demonstrate this approach. Over 1400 Computer-aided design (CAD) models of different configurations are developed based on the description from [23]. In-vitro EM simulations are performed to obtain the 1g SARs (corresponding to the RF-induced heating) for all these configurations. The combined meshes and the incident electric fields are used as the input for

\*Jiajun Chang, Ran Guo, Jianfeng Zheng, Stuart Long, and Ji Chen are with the University of Houston, Houston, TX 77204 USA (e-mail: jchen18@uh.edu). Qianlong Lan was with the University of Houston. He is now with eBay Inc. (e-mail:lq11254@gmail.com); Wolfgang Kainz was with Laboratories, Center for Devi Administration, Silver Spring for MRI Safety, LLC (e-mail:

Rebeca Romero is with Arthrex, 1370 Creekside Blvd, Naples, FL 34108 (email: Rebeca.Romero@Arthrex.com).

Wolfgang Kainz was with the Office of Science and Engineering Laboratories, Center for Devices and Radiological Health, Food, and Drug Administration, Silver Spring, MD 20993-0002 USA. He is now with HPC for MRI Safety, LLC (e-mail: mrisafety@hpcmris.com).

This paper is an expanded version from the Q. Lan, J. Zheng, J. Chang, R. Guo, W. Kainz and J. Chen, "Predicting MRI RF Exposure for Passive Implantable Medical Devices Using a Mesh-based Convolutional Neural Network," 2021 IEEE International Symposium on Antennas and Propagation and USNC-URSI Radio Science Meeting (APS/URSI), 2021, pp. 1493-1494, doi: 10.1109/APS/URSI47566.2021.9704709.

the CNN model, and the peak value of 1-gram spatial-averaged Specific Absorption Rate (SAR) extracted from the simulations are used as the outputs of the CNN model. During the CNN model development, the network convergence and the correlations between predicted and true 1g SARs are continuously monitored. Error metrics such as mean absolute error (MAE) and Mean Absolute Percentage Error (MAPE) are used to ensure the convergence (MAPE less than 5%) of the CNN model. The strategy for choosing an optimum size for the training dataset is also addressed and discussed with the assistance of Principal Component Analysis (PCA).

The rest of this article is organized as follows. In Section II, CAD models of the tibia plate system are introduced, and invitro simulations are performed on these systems. In Section III, the settings for the CNN model are elaborated. Section IV presents the results of the CNN model development and the network's effectiveness for the RF-induced heating of various complex-shaped PIMDs. Further discussion is provided in Section V, and Section VI gives the overall conclusions.

#### II. METHODOLOGY

## A. Development of CAD models

CAD models are developed based on distal tibia plating systems that treat distal tibia bone fracture from a commercial PIMD manufacturer [23] designed to treat distal tibia bone fractures. Screws can be applied at various positions on the plate to provide stability and rigidity. The four types of tibia plating systems that were selected for computational modeling are the anterolateral, medial, anterior, and posterior systems. Illustrations of these devices are shown in Fig. 1. CAD models of the plate systems are developed using SEMCAD X (14.8.1, SPEAG, Zurich, Switzerland). The front, side, and top views of the CAD models are shown in Fig. 2. Cortical screws are applied in the diaphysis (shaft) while cancellous screws are used in the epiphysis region for fixations.

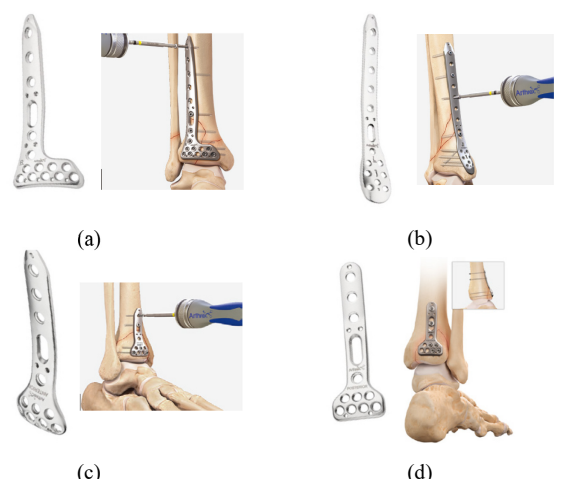


Fig. 1. Four types of CAD models developed with the SEMCAD software package and illustration of the numbering of screw holes in the epiphysis region.

As shown in Fig. 2, these plates have various shapes that cannot be easily described by a fixed set of geometrical

parameters. For these plates, the overall lengths range from 62 mm to 278 mm. Screws of different lengths, diameters, and numbers can be applied to the screw holes illustrated in the figure. For this application, screws with a diameter of 3.5 mm are used in the diaphysis, and screws with a diameter of 2.7 mm are used in the epiphysis region. For both screw diameters, the screws have three distinct lengths of 10 mm, 30 mm, and 60 mm. In the diaphysis region, one screw should be applied to the center positioning hole and the other screws will be applied at either the top or the bottom screw hole. For the screw holes in the epiphysis region, the screw holes are numbered as 1,2,3, etc from top left to bottom right as shown in Fig. 2. The number of screws is randomly selected and placed into different holes for each configuration. The length of each screw is also randomly selected from the three possible lengths. Over 1400 configurations are developed for all four tibia plate systems. The details of the configurations are shown in TABLE I.

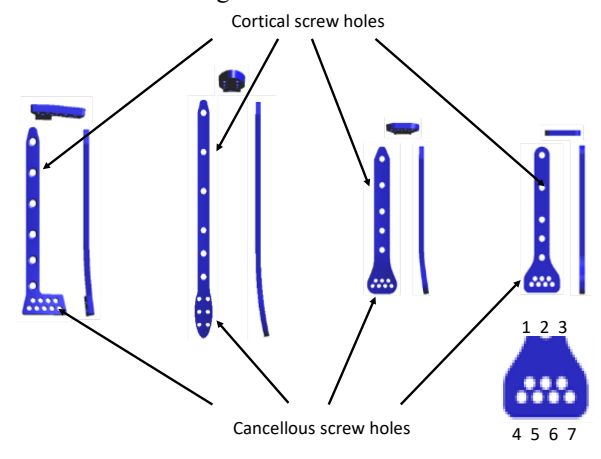


Fig. 2. Four types of plate CAD models developed with the SEMCAD software package and illustration of the numbering of screw holes in the epiphysis region.

#### B. In-vitro Simulations

In-vitro simulations are performed using the SEMCAD X, an EM simulation software package based on the finite-difference time-domain (FDTD) method for all four tibia plate systems. A generic birdcage coil, which consists of eight current sources on eight rungs of the coil and sixteen lumped elements in the top and bottom end rings, is used as the RF excitation in simulations [6][24]. The operating frequency of the coil is 64 MHz which corresponds to the 1.5T MRI system.

In the in-vitro simulations, the devices are placed inside the standard ASTM phantom [7]. The phantom is filled with gelled saline of 90 mm in depth with a relative permittivity of 80 and electrical conductivity of 0.47 S/m. The ASTM phantom shell is made of acrylic material with a relative permittivity of  $\epsilon_r = 3.7$  and electrical conductivity of  $\sigma = 0$  S/m. All device centers are placed at the center location on the *z-axis* and the *y-axis* in the phantom as shown in Fig. 3. The device screws are oriented along the negative x-direction. The right edge of the device is 20 mm from the sidewall of the ASTM phantom. The ASTM phantom trunk center is placed at the isocenter of the RF coil as shown in Fig. 3. This procedure is applied for all four different plates during the simulation setups.

TABLE I
TOTAL PLATE CONFIGURATIONS

Plate type	Plate length (mm)	Screw length (mm)	Screw position for diaphysis (shaft) region (screw diameter 3.5 mm)	Screw position for epiphysis region (screw diameter 2.7 mm)	
Anterolateral	[66,91,117,142,168,19 3,218,244]			{[1,2,4,5,9], [1,3,4,5,9], [1,4,5,8,9], [1,4,5,7,9], [1,4,5,8,9], [1,2,3,4,5,6,7,8,9]}	
Medial	[103,128,154, 179,204,230,278]	[10,30,60]	{[top hole, positioning hole],	{[2,3,5,6], [1,3,4,6], [1,2,4,5], [1,2,3,4,5,6]}	
Anterior	[62,84,107,130]		[mid hole, positioning hole]}	{[1,3,4,7], [1,2,3,4,7], [1,3,4,5,7], [1,3,4,6,7], [1,2,3,4,5,6,7]}	
Posterior	[57,77,98,118]			{[1,3,4,7], [1,2,3,4,7], [1,3,4,5,7], [1,3,4,6,7], [1,2,3,4,5,6,7]}	

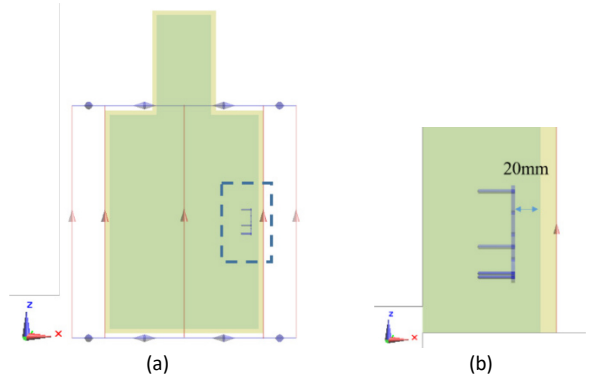


Fig. 3. Illustration of the device placement inside the ASTM phantom and the RF coil. (a) Device placement inside ASTM phantom, (b) Detailed illustration of the device placement.

To ensure the convergence of EM simulations, the minimum FDTD simulation time should be at least 20 periods. Since these plates are made of metallic materials such as stainless steel or titanium, they are modeled as perfect electric conductors (PECs). The mesh step size is set to 10 mm in the ASTM phantom shell and to 5 mm in the gelled saline filling. To ensure all plate devices have the same mesh as the input of the CNN model, a large grid mask is applied to contain all the different configurations. The grid mask is 70 mm × 50 mm × 290 mm, and, devices of different configurations are placed inside this region. In all simulations, the grid mask has a resolution of 0.8 mm in the x, y, and z directions so that all fine features from the PIMDs can be accurately represented by the electromagnetic meshes. Overall, the global mesh has a size of  $190 \times 108 \times 100$  $511 = 10.48 \,\mathrm{M}$  cells, as shown in Fig. 4. This mesh is used in both the electromagnetic simulations and as the input for the CNN model.

After all the simulations are completed, postprocessing is needed to obtain meshes, incident field distribution, and the RF-induced heating data (in terms of peak 1 gram spatial-averaged SAR) for each simulation. Due to the conductivity loss of the

gel, the SAR distribution will be concentrated in the device region Consequently, only the mesh information inside the grid mask is extracted in preparing for the CNN training. The electromagnetic simulation mesh for each simulation is a 3-D matrix with  $89\times65\times364\approx2.1$  million elements. Since there are two materials inside the grid mask, element 0 is used to represent gelled saline and element 1 is used to represent the devices. The mesh matrix for each simulation is defined as *Mesh* whose element is either 0 or 1.

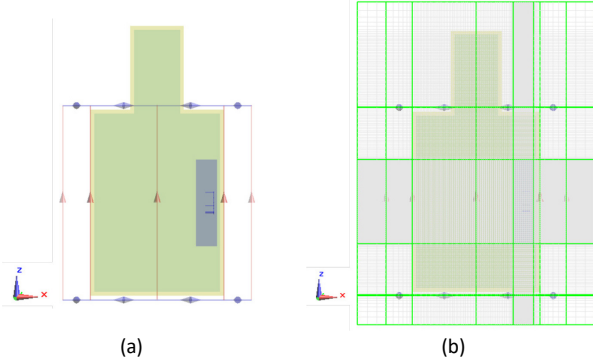


Fig. 4. Illustration of (a) the grid mask to enclose all devices, and (b) the mesh setup for all simulations.

The incident electric fields in the grid mask are then extracted from the simulations. Since the z-directional electric field is the dominant component [4][5], the incident electric field is approximated as

$$E_{incz}(i,j,k) = \hat{z} \cdot \mathbf{E}_{inc}(i,j,k)$$
 (1)

where  $E_{inc}(i.j,k)$  is the total incident electric field at the discretized grid location (i.j,k), z is the unit vector in z direction and  $E_{incz}(i.j,k)$  is the z-component of the incident electric field.

Since the resultant SAR is mainly related to the scattered electric fields from the metallic implants, in this study, we only record the incident field on the metallic mesh for CNN data preparation. This is achieved by combining the mesh

information and the incident electric field information, elementwise multiplications are performed between  $E_{inc}$  and Mesh. The multiplication result will retain the original  $E_{inc}$  value at the metallic implant region and will be 0 for the conductive gel region as described as:

$$\begin{split} E_{mesh}(i,j,k) &= E_{incz}(i,j,k) \times Mesh(i,j,k) \\ &= \begin{cases} E_{incz}(i,j,k), & implants \\ 0, & phantom \ gel \end{cases} \end{split} \tag{2}$$

This leads to a complex number at the device grid location. The magnitude of the  $E_{\text{mesh}}$  slices at several depths in the *y*-direction are shown in Fig. 5.

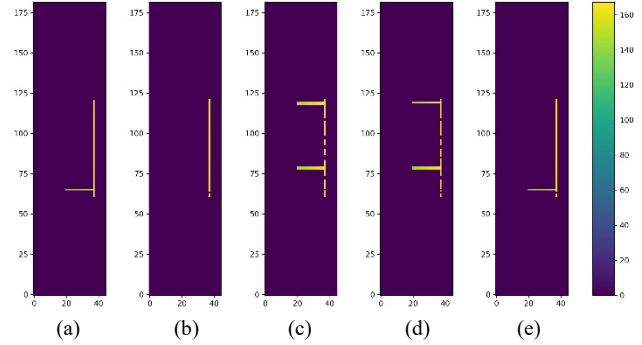


Fig. 5. Illustration of x-z slices of the E\_mesh matrix at different y positions: (a) y = -1.56 mm, (b) y = -0.58 mm, (c) y = 0 mm, (d) y = 0.78 mm and (e) y = 1.56 mm.

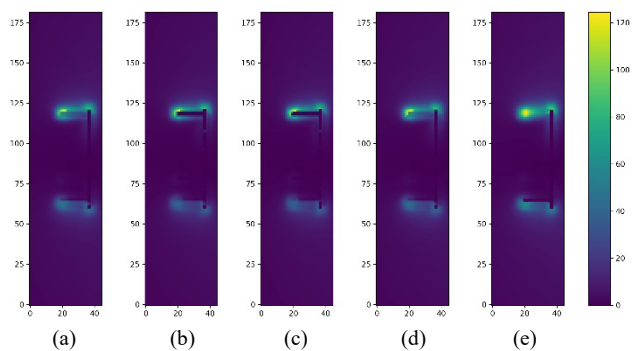


Fig. 6. Illustration of x-z slices of the 1g SAR distributions at different y positions: (a) y = -1.56 mm, (b) y = -0.58 mm, (c) y = 0 mm, (d) y = 0.78 mm and (e) y = 1.56 mm.

Overall, more than 1,400  $E_{mesh}$  matrices and the corresponding  $SAR_{1g}$  values are extracted and form the dataset used for training and testing the CNN model. The SAR distributions corresponding to the slices in Fig. 5 are given in Fig. 6. To estimate the worst-case heating, only peak spatial averaged SAR (psSAR<sub>1g</sub>) is required as the output for the CNN training. In most cases, the psSAR<sub>1g</sub> values are located near the tip of the screws or the edges of the plate.

## III. CONVOLUTIONAL NEURAL NETWORK MODEL

#### A. Network Overview

The sequential CNN model used in this study is derived from AlexNet [26]. The illustration of the network structure is shown in Fig. 7. The network consists of one input layer, two convolutional layers, two max-pooling layers, one flatten layer, two fully connected layers, and one output layer. Convolutional

layers and max-pooling layers operate on 3-D data which will be flattened to a 1-D vector by flattening the layer and then going through the fully connected layers.

# B. Network Configurations

To reduce the complexity of the CNN model, the input  $E_{mesh}$  matrix is decimated by a factor of 2 in all three directions. The  $E_{mesh}$  size is now reduced  $45 \times 33 \times 182$ . In addition, since the  $E_{mesh}$  matrices cannot be directly used as the input to the CNN model, appropriate pre-processing is needed to convert it into a larger interleaved real-valued 3D matrice called  $E_{Rmesh}$ . Each element in the  $E_{Rmesh}$  is defined as

$$\begin{cases} E_{\text{Rmesh}}(2 \cdot (i-1)+1,j,k) = Real(E_{\text{mesh}}(i,j,k)) \\ E_{\text{Rmesh}}(2 \cdot i,j,k) = Imag(E_{\text{mesh}}(i,j,k)) \end{cases}$$
(3)
$$= \begin{cases} E_{\text{Rmesh}}(2 \cdot i,j,k) = Imag(E_{\text{mesh}}(i,j,k)) \\ E_{\text{Rmesh}}(2 \cdot i,j,k) = Imag(E_{\text{mesh}}(i,j,k)) \end{cases}$$
(3)

Fig. 7. Illustration of the CNN architecture used in the study. The CNN model consists of one input layer, two convolutional layers, two max-pooling layers, one flatten layer, two fully connected layers, and one output layer.

After this operation, the total size of  $E_{Rmesh}$  is 90 × 33 × 182. In the two convolutional layers, different filters with a size of  $6 \times 2$  are applied to extract the features of the input layers. Each filter will slide through each input layer and the output will be the dot-product of the filter kernel weights and the element values inside a small region covered by the filter. As a default, the filters slide along the input elements one by one both horizontally and vertically. To keep the integrity of the complex number information, the stride, which is the slide step size for filters, is set to two in the concatenated direction such that all 12 values cover six complex numbers. Both convolutional layers have 80 filters which will produce 80 feature maps after convolution operations. Illustrations of some feature maps after the convolutional layers are shown in Fig. 8. As shown in the Fig. 8, geometrical information for a typical device is extracted.

After each convolutional layer, a max-pooling layer is created by selecting the maximum value in a  $2 \times 2$  area to reduce the size of the input layer while keeping the important features. The flatten layer converts all 2-D feature maps to a 1-D vector. Three flatten layers and fully connected layers have 350, 256, and 128 neurons respectively. The last layer (output layer) reduces to a single element which corresponds to the psSAR<sub>1g</sub>. During network training, back propagations are performed to update the weights in the entire system to minimize the error level between the true values and the CNN predicted values.

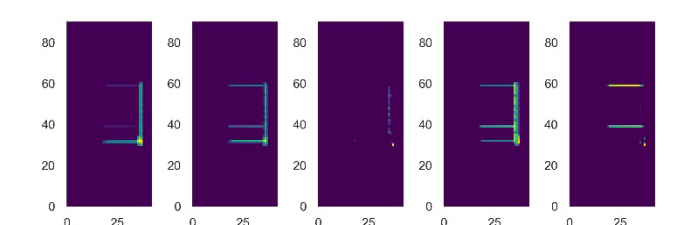


Fig. 8. Illustration of the output 2-D feature maps after two convolutional layers and two max-pooling layers.

# C. Error/Convergence Analysis

The architecture construction, network training, testing, and evaluation of the results are all implemented in Python with Keras [27]. For the loss function, the Mean Absolute Percentage Error (MAPE) is selected which is defined as follows:

$$MAPE = \frac{100\%}{n} \sum_{t=1}^{n} \left| \frac{A_t - F_t}{A_t} \right| \tag{4}$$

where  $A_t$  is the true value,  $F_t$  is the CNN predicted value, and n is the number of data points. In addition, the Mean Absolute Error (MAE) is defined as:

$$MAE = \frac{1}{n} \sum_{t=1}^{n} |A_t - F_t|$$
 (5)

The entire dataset is divided into a training dataset and a testing dataset, with 70% of the datasets randomly selected as training datasets and the remaining 30% considered as testing datasets. Within the training dataset, 20% are chosen as validation datasets, whose error metrics will be evaluated through training while the dataset itself will not be used in network training. The overall percentage allocation is 56%:14%:30% for training, validation, and testing respectively.

The Adam algorithm [28] is chosen as the optimizer of the network. Training epochs are set to 100, and batch size is set to 32.

#### IV. RESULTS

#### A. Convergence and Correlation

The total duration for 100 epochs of the CNN model training is around 15 minutes. The time consumption comparison between traditional EM simulation and the proposed technique is conducted and shown in TABLE II. The time needed to run 1416 EM simulations is 873.2 hours. For the proposed CNN model, since 70% of the EM simulations are needed for data training, 611.2 hours are taken for running those simulations. The training of the CNN model takes 15 minutes and the prediction takes less than 1 second. Thus, the total time is saved by 30% by using the prosed model. During the network training process, MAPE is evaluated at every epoch.

TABLE II
TIME CONSUMPTION(UNIT: HOUR)

	Data Preparation	Model Training	Data Prediction	Total
EM Simulation	873.2	/	/	873.2
Proposed Technique	611.2	0.25	< 0.001	611.49

The MAPE of the training datasets and the validation datasets is shown in Fig. 9. It can be seen that the error level decreases

abruptly in the first ten epochs. After that, the error level fluctuates at the level of 5% while still decreasing slowly. Also, the validation MAPE is close to the training MAPE, which means that the network is robust to the new data, and that there is no overfit for the CNN model.

Once the network training is finished, the psSAR<sub>1g</sub>, MAE, and MAPE values of the training dataset (including validation data), and of the testing dataset are tabulated in TABLE III. It shows that the averaged psSAR<sub>1g</sub> value for both training and testing datasets is around 200 W/kg, the MAE is less than 5 W/kg, and the MAPE is less than 3%. These errors are similar for both the training and validation datasets.

The correlation coefficient between the predicted psSAR<sub>1g</sub> values and true psSAR<sub>1g</sub> values of the training and testing datasets are evaluated using the R2 score, which is defined as:

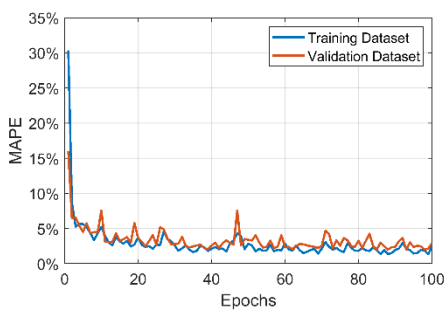


Fig. 9. Illustration of the change of MAPE level during 100 epochs of network training for the training and validation datasets.

TABLE III MEAN SAR, MAE, AND MAPE

lue	Averaged SAR v	
	(W/kg)	
	MAE (W/kg) MAPE	
_ 1		
$-\frac{\sum_{i}(1-\sum_{i}(1-\frac{\sum_{i}(1-\sum_{i}(1-\frac{\sum_{i}(1-\sum_{i}(1$	2.	

(6)

where  $y_i$  is the true value,  $f_i$  is the predicted value, and  $\bar{y}$  is the averaged true value. The plots of predicted values vs true values for both the training and testing datasets are shown in Fig. 10. Both the training and testing datasets have an R2 score of 0.99. It can be seen from the scatter plots that the majority of the data points are close to the y=x line on which the predicted value and true value are equal to each other. Only a few data points deviate from the y=x line.

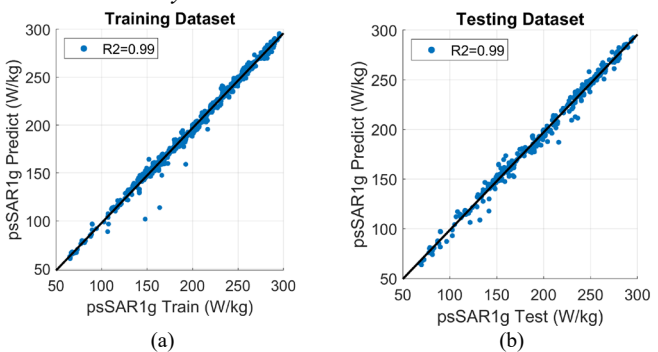


Fig. 10 Illustration of correlations between predicted values and true values of (a) training dataset and (b) testing dataset.

B. Error Distribution V. DISCUSSION

Firstly, the distribution of the peak SAR values for both datasets are investigated and the histograms of distribution are shown in Fig. 11. It can be obtained from the figure that, the peak SAR values of the plate devices are concentrated with the range of [90W/kg, 300W/kg] while the range of [150W/kg, 200 W/kg] has the largest number of occurrences. There are also no outliers for peak SAR values.

Histograms of MAE for the training dataset and the testing dataset are shown in Fig. 12. From the figure, the majority of the training and testing data has an MAE value of less than 10 W/kg. The maximum MAE value for the training dataset is 50.04 W/kg, and the maximum MAE value for the testing dataset is 29.03 W/kg.

Histograms of MAPE for the training and testing datasets are shown in Fig. 13. It can be observed that the majority of data has a MAPE level of less than 5%. The maximum MAPE of the training dataset is 31%, and the maximum MAPE of the testing data is 17.77%. All these observations demonstrate the effectiveness of this method.

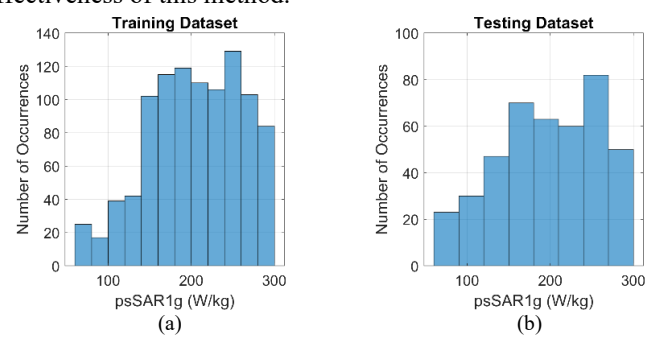


Fig. 11. Illustration of psSAR<sub>1g</sub> distribution for (a) the training dataset, and (b) the testing dataset

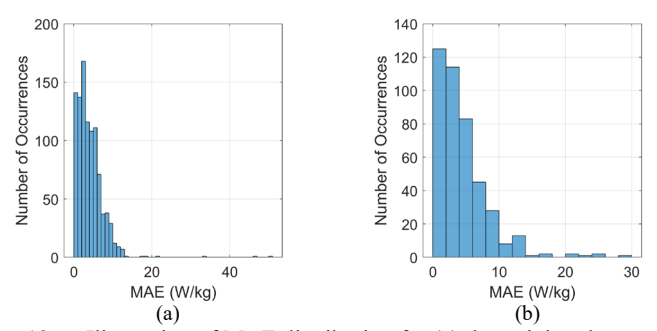


Fig. 12. Illustration of MAE distribution for (a) the training dataset, and (b) the testing dataset

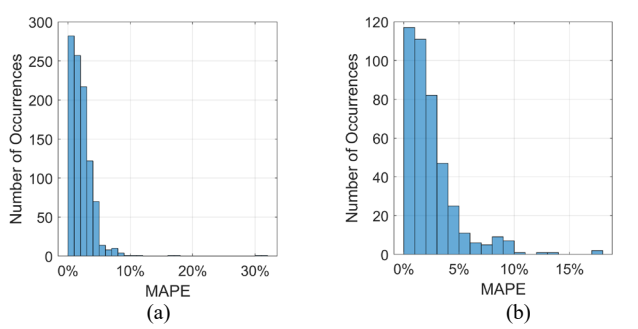


Fig. 13. Illustration of MAPE distribution for (a) training dataset and (b) testing dataset.

# A. Training Data Selection

From the results given in the previous section, the CNN model can achieve good convergence when it is used to predict the RF-induced heating from PIMDs. The predicted  $psSAR_{1g}$  and true  $psSAR_{1g}$  have a good correlation coefficient of  $R^2$ =0.99.

In the previous training scenarios, 70% of the total datasets is used to form the training datasets. However, obtaining 70% of all configurations for the training dataset development requires extensive electromagnetic simulations for almost one month, even with GPU acceleration. Therefore, it is necessary to determine the least possible amount of training datasets that can be used and still achieve a good prediction.

To perform this study, 20% of the whole datasets are randomly selected as testing data. The CNN models are then trained using 10% to 80% (with an increment of 10%) of the datasets randomly selected from the original datasets. The validation dataset is always 20% of the randomly selected training set. The CNN models are trained 50 times in each study.

TABLE IV shows the correlation coefficient R<sup>2</sup>, MAE, and MAPE values with different sizes of the training datasets. Also, the maximum errors appeared among 50 trainings are evaluated and shown. It can be seen that when the training datasets are less than 20% of the total datasets, errors are relatively large, and the R<sup>2</sup> score is low. However, these parameters are drastically improved when the training dataset size reaches 30% of the total datasets. However, there are no significant improvements when one further increases the size of the training datasets. The maximum error has the similar trend which the error level decreases significantly from 30% of the dataset and keep stable. Based on this study, it appears that only 30% of the original datasets can be used and still develop a CNN model with accurate psSAR<sub>1g</sub> predictions for the tibia plate systems. Noted that, although the max error level is significant, it is a singular value from one data prediction from one of fifty trainings, which means that the maximum error is expected to be lower.

# B. Error Threshold Indicated by Principal Component Analysis (PCA)

The results in the previous section indicate that it is feasible to use a small subset of datasets to develop a satisfactory CNN model to predict RF-induced heating for tibia plate systems. It is also observed once the size of the datasets exceeded a certain number, there is no additional improvement in terms of the CNN model accuracy. Therefore, the objective here is to perform the principal component analysis (PCA) on the input dataset [29]. The PCA algorithm extracts the Principal Components (PCs), and the variance for each PC which represents the significance of the PCs to represent the whole data.

An  $E_{mesh}$  with a size of  $45 \times 33 \times 182$  is reshaped into 1-D complex vectors with a length of 270,270 for over 1400 plate configurations. Then, the PCA is performed on the matrix reshaped at  $270,270 \times 1416$ . Such a PCA takes about 20

minutes to perform. Once the PCA is finished, the PCs are extracted and are ranked based on the variance of each PC.

Fig. 14 shows the PCs distributions of the 1<sup>st</sup>, 11<sup>th</sup>, 21<sup>st</sup>, 31<sup>st</sup>, and 41<sup>st</sup> largest variances after the PCA. These 2-D distributions correspond to the center plane in the original simulation grids. As seen in the figure, the largest component has large values

along the vertical direction. As the variance becomes smaller, larger values are along the horizontal direction. This observation further confirms that the components along the vertical direction would contribute significantly toward the RF-induced heating for these PIMDs.

TABLE IV
R <sup>2</sup> , MAE, AND MAPE ON DIFFERENT TRAINING DATASET SIZE

data (%)	Training	Training Dataset			Testing Dataset				
	data amount	MAE (W/kg)	MAPE (%)	$\mathbb{R}^2$	Max Error (W/kg)	MAE (W/kg)	MAPE (%)	$\mathbb{R}^2$	Max Error (W/kg)
10%	142	11.52	5.94	0.91	66.4	14.64	8.19	0.88	72.6
20%	283	11.33	5.66	0.93	66.3	12.43	6.80	0.92	73.7
30%	425	4.43	2.31	0.98	55.7	5.78	3.30	0.97	59.0
40%	566	5.61	2.88	0.98	61.0	6.26	3.52	0.98	53.7
50%	708	4.98	2.57	0.98	60.0	5.70	3.19	0.98	47.5
60%	805	4.35	2.23	0.98	54.6	4.89	2.70	0.98	47.2
70%	991	4.94	2.51	0.98	50.9	5.18	2.84	0.98	42.0
80%	1133	4.87	2.42	0.98	56.4	5.10	2.73	0.98	45.8

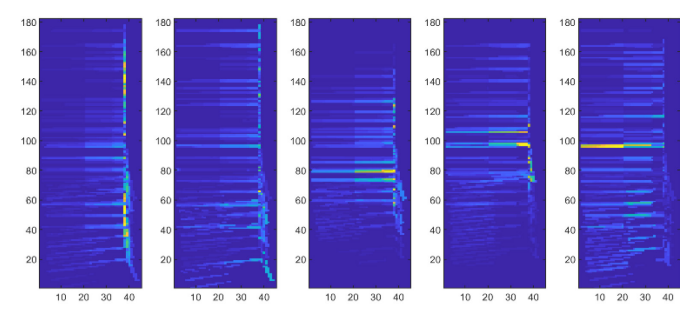


Fig. 14. Illustrations of the PCs at the center of the 1st, 11th, 21st, 31st, and 41st largest variance.

One potential criterion for selecting the size of the datasets can be performed through cumulative variance analysis. The ratio between the cumulative sum of the first *n* PCs' variances and the sum of all variances, defined as the Cumulative Explained Variance (CEV) is shown in Fig. 15. As seen in the figure below, one can represent the original datasets with the largest 400 PCs. Consequently, if only 400 datasets are selected, it is possible to train the CNN model with good accuracy with such a subset of the training datasets.

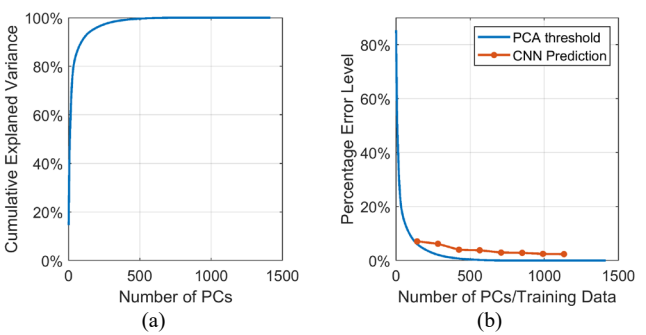


Fig. 15. (a) Illustration of cumulative explained variances for 1416 PCs, and (b) Comparison between CNN prediction error and PCA threshold.

The 1-CEV(n) indicates the percentage of the total energy that

is not included in the datasets for the CNN model development, which is defined as follows:

$$1 - CEV(n) = 1 - \frac{cumsum(\sigma)}{sum(\sigma)} = 1 - \frac{\sum_{i=1}^{n} \sigma_i}{\sum_{i=1}^{N} \sigma_i}$$
 (7)

where  $\sigma_i$  is the variance of *i*th PC. This would be the lowest level that a CNN model can achieve. Fig. 15 (b) shows the 1–CEV(n) and the CNN prediction error as the training datasets increase. As the size of the training dataset increases, both the 1–CEV(n) and the MAPE of the CNN model decrease. However, as expected, the MAPE would be still higher than the 1–CEV(n). For the RF-induced heating for the tibia plates used in this study, based on the 1–CEV(n), it appears that the size of 400 datasets is a good indication that all energy that has been included in the training sets. However, the error levels from the CNN model are still slightly higher than the 1–CEV(n).

Based on previous results, 1–CEV(*n*) can be used as a reference for choosing the appropriate training dataset size. The percentage error calculated from the PCA can be considered as the lower limit of the prediction error from the CNN model. For example, to achieve a MAPE level of 10%, the training dataset must contain at least 100 datasets, as 100 PCs will produce a 10% error level. Overall, the PCA can be used as an assistant tool to estimate the required size of the training datasets.

# VI. CONCLUSIONS

In this paper, a CNN model is proposed for the prediction of RF-induced heating of complex-shaped PIMDs. In-vitro EM simulations are performed with 1416 tibia plate configurations with different geometrical variations. After that, the 3-D device mesh information is combined with the local incident electric field information and used as the input of the CNN model. Good convergence was achieved and an over 0.99 correlation coefficient for both training and testing datasets was obtained, indicating the accuracy of the CNN model. The PCA on the input data can be used as a potential criterion for selecting an

appropriate dataset for network training. Overall, it was demonstrated that the mesh-based CNN model can be used for quick access to the RF-induced heating for complex-shaped PIMDs under MRI.

#### ACKNOWLEDGMENT

The mention of commercial products, their sources, or their use in connection with material reported herein is not to be construed as either an actual or suggested endorsement of such products by the Department of Health and Human Services.

## REFERENCES

- [1] A. Kiourti and K. S. Nikita, "A Review of In-Body Biotelemetry Devices: Implantables, Ingestibles, and Injectables," IEEE Transactions on Biomedical Engineering, vol. 64, no. 7, pp. 1422-1430, 2017.
- [2] F. G. Shellock and J. V. Crues, "MR Procedures: Biologic Effects, Safety, and Patient Care" *Radiology*, vol. 232, no. 3, pp. 635-652, 2004.
- [3] W. Kainz, G. Neubauer, R. Überbacher, F. Alesch, and D. D. Chan, "Temperature Measurement on Neurological Pulse Generators during MR scans" BioMedical Engineering OnLine, vol. 1, no. 1, pp. 1-8, 2002.
- [4] Y. Liu, J. Chen, F. G. Shellock and W. Kainz, "Computational and Experimental Studies of an Orthopedic Implant: MRI-related Heating at 1.5-T/64-MHz and 3-T/128-MHz," *Journal of Magnetic Resonance Imaging*, vol. 37, no. 2, pp. 491-497, 2013.
- [5] Nordbeck, Peter, Florian Fidler, Ingo Weiss, Marcus Warmuth, Michael T. Friedrich, Philipp Ehses, Wolfgang Geistert et al. "Spatial distribution of RF-induced E-fields and implant heating in MRI." Magnetic Resonance in Medicine: An Official Journal of the International Society for Magnetic Resonance in Medicine 60, no. 2 (2008): 312-319.
- [6] J. Zheng, D. Li, J. Chen and W. Kainz, "Numerical Study of SAR for Multi-component Orthopedic Hip Replacement System during MRI," in 2016 IEEE International Symposium on Electromagnetic Compatibility, Ottawa, 2016.
- [7] ASTM F2182-19e2a, "Standard Test Method for Measurement of Radiofrequency Induced Heating On or Near Passive Implants During Magnetic Resonance Imaging," ASTM, 2019.
- [8] R. Guo, M. Chen, J. Zheng, R. Yang, J. Chen and W. Kainz, "Comparison of In-vivo and In-vitro MRI RF Heating for Orthopedic Implant at 3 Tesla," in 2017 IEEE International Symposium on Electromagnetic Compatibility & Signal/Power Integrity, Washington, DC, 2017.
- [9] X. Ji, J. Zheng, and J. Chen, "Numerical Evaluation of RF-induced Heating for Various Esophageal Stent Designs Under MRI 1.5 Tesla System," Electromagnetic Biology and Medicine, vol. 36, no. 4, pp. 379-386, 2017.
- [10] R. Guo, J. Zheng, Y. Wang, Q. Zeng, Q. Wang, R. Yang, W. Kainz, and J. Chen, "Computational and Experimental Investigation of RF-induced Heating for Multiple Orthopedic Implants," Magnetic Resonance in Medicine, vol. 82, no. 5, pp. 1848-1858, 2019.
- [11] J. Zheng, M. Xia, W. Kainz, and J. Chen, "Wire-based Sternal Closure: MRI-related Heating at 1.5 T/64 MHz and 3 T/128 MHz Based on Simulation and Experimental Phantom Study," Magnetic Resonance in Medicine, vol. 83, no. 3, pp. 1055-1065, 2019.
- [12] Qi-Jun Zhang, K. C. Gupta and V. K. Devabhaktuni, "Artificial Neural Networks for RF and Microwave Design - from Theory to Practice," IEEE Transactions on Microwave Theory and Techniques, vol. 51, no. 4, pp. 1339-1350, 2003.
- [13] V. K. Devabhaktuni, C. Xi, F. Wang, and Q.-J. Zhang, (2002), "Robust Training of Microwave Neural Models," *International Journal of RF and Microwave Computer-Aided Engineering*, vol. 12, no. 3, pp. 109-124, 2001.
- [14] F. Wang and Q.-J. Zhang, "Knowledge-based Neural Models for Microwave Design," IEEE Transactions on Microwave Theory and Techniques, vol. 45, no. 12, pp. 2333-2343, 1997.
- [15] J. Xu, M. C. E. Yagoub, R. Ding, and Q.-J. Zhang, "Neural-based Dynamic Modeling of Nonlinear Microwave Circuits," IEEE Transactions on Microwave Theory and Techniques, vol. 50, no. 12, pp. 2769-2780, 2002.

- [16] M. Vai and S. Prasad, "Microwave Circuit Analysis and Design by A Massively Distributed Computing Network," IEEE Transactions on Microwave Theory and Techniques, vol. 43, no. 5, pp. 1087-1094, 1995.
- [17] J. Zheng, R. Yang and J. Chen, "Fast Prediction of MRI RF-induced Heating for Implantable Plate Devices using Neural Network," in 2017 IEEE International Symposium on Antennas and Propagation & USNC/URSI National Radio Science Meeting, San Diego, 2017.
- [18] J. Zheng, Q. Lan, X. Zhang, W. Kainz, and J. Chen, "Prediction of MRI RF Exposure for Implantable Plate Devices Using Artificial Neural Network," IEEE Transactions on Electromagnetic Compatibility, vol. 62, no. 3, pp. 673-681, 2020.
- [19] J. Vu, B. T. Nguyen, B. Bhusal, J. Baraboo, J. Rosenow, U. Bagci, M. G. Bright, and L. Golestanirad, "Machine Learning-Based Prediction of MRI-Induced Power Absorption in the Tissue in Patients With Simplified Deep Brain Stimulation Lead Models," IEEE Transactions on Electromagnetic Compatibility, vol. 63, no. 5, pp. 1757-1766, 2021.
- [20] Q. Lan, J. Zheng, and J. Chen, "Predicting MRI RF Exposure for Complex-shaped Medical Implants Using Artificial Neural Network," in 2019 IEEE International Symposium on Antennas and Propagation and USNC-URSI Radio Science Meeting, Atlanta, 2019.
- [21] D. Li, J. Zheng, Y. Liu, C. Pan, W. Kainz, F. Yang, W. Wu and J. Chen, "An Efficient Approach to Estimate MRI RF Field-Induced In Vivo Heating for Small Medical Implants," *IEEE Transactions on Electromagnetic Compatibility*, vol. 57, no. 4, pp. 643-650, 2015.
- [22] Q. Lan, J. Zheng, J. Chen and M. Zhang, "Prediction of MRI RF-induced Heating for Passive Implantable Medical Devices Using Convolutional Neural Network," in 2020 IEEE International Symposium on Electromagnetic Compatibility & Signal/Power Integrity (EMCSI), Reno, 2020.
- [23] Arthrex, "Distal Tibia Plating System," [Online]. Available: https://www.arthrex.com/foot-ankle/distal-tibia-plating-system.
- [24] J. Chen, Z. Feng, J. Jin, "Numerical simulation of SAR and B1-field Inhomogeneity of Shielded RF Coils Loaded with the Human Head," IEEE Transactions on Biomedical Engineering, vol. 45, no. 5, pp. 650-659, 1998.
- [25] IEEE P62704-1, "Standard for Determining the Peak Spatial Average Specific Absorption Rate (SAR) in the Human Body from Wireless Communications Devices, 30 MHz to 6 GHz. Part 1," IEEE, 2020
- [26] A. Krizhevsky, I. Sutskever and G. Hinton, "Imagenet Classification with Deep Convolutional Neural Networks," *Advances in neural information processing systems*, vol. 25, pp. 1097-1105, 2012.
- [27] F. Chollet, "Keras," 2015. [Online]. Available: https://github.com/fchollet/keras.
- [28] D. Kingma and B. Jimmy, "Adam: A Method for Stochastic Optimization," arXiv preprint arXiv, vol. 1412, no. 6980, 2014.
- [29] I. T. Jolliffe, and J Cadima. "Principal Component Analysis: A Review and Recent Developments," *Philosophical transactions. Series A, Mathematical, physical, and engineering sciences*, vol. 374, no. 2065, 2016.